PERGAMON

International Journal of Solids and Structures 37 (2000) 3305–3322

INTERNATIONAL JOURNAL OF SOLIDS and STRUCTURES

www.elsevier.com/locate/ijsolstr

Validity of one-dimensional experimental principle for flat specimen in bar–bar tensile impact apparatus

C.Y. Wang, Y.M. Xia*

Department of Modern Mechanics, University of Science and Technology of China, Hefei, Anhui 230027, People's Republic of China

Received 3 December 1997; in revised form 21 December 1998

Abstract

The Bar–bar Tensile Impact Apparatus (BTIA) is widely used to measure the dynamic tensile properties of solid materials. In the present paper, a simplified three-dimensional finite element model for the BTIA system with a flat specimen is established to simulate the experimental process of a BTIA. The numerical solution for the model is solved by ADINA. In the scope of elastoplastic theory, the numerical analysis confirms the validity of the one-dimensional experimental principle used in the BTIA, as long as certain foundations are satisfied.

Keywords: Stress wave; Bar–bar Tensile Impact Apparatus (BTIA); Three-dimensional finite element analysis; Dumb-bell-like flat specimen

1. Introduction

Kolsky (1949) first developed the modern Split Hopkinson Pressure Bar (SHPB) apparatus in 1949. At present SHPB, as shown in Fig. 1, has been widely used to study the dynamic properties of solid materials. In the 1960's and 1970's, a number of researchers conducted a large amount of theoretical and experimental research work in order to improve the SHPB technique and extend its usage. Bertholf (1974) and Bertholf and Karnes (1975) produced a two-dimensional axisymmetric numerical analysis for SHPB. They studied the influences on the experimental results of the specimen geometry and friction between the specimen and the input/output bar, and gave the matching relation between the specimen and the SHPB system that made the experimental measuring principle valid under small friction. Bertholf's work laid a solid theoretical foundation for the SHPB technique.

* Corresponding author. Fax: 86-551-3631760.
E-mail address: ymxia@ustc.edu.cn (Y.M. Xia).

0020-7683/00/$ - see front matter
PII: S0020-7683(99)00035-9

In recent decades, various tensile impact apparatuses have been developed one after another. The Bar–Bar Tensile Impact Apparatus (BTIA) is the chief form. Xia et al. (1992, 1996) developed the rotation disk tensile impact test apparatus. As shown in Fig. 1, when the hammer on the high-speed rotation disk (the disk is not shown in the figure) impacts on the block, the short metal bar (made of aluminum) is broken, which produces an approximately rectangular input stress impulse wave. Making use of the plastic flow of the short metal bar, the oscillation in the incident impulse, compared with the general way of using the hammer to impact directly on the block, is filtered a great deal. This technique can make the incident impulse very smooth, which enhances the accuracy of the experimental results.

The experimental principle of BTIA is the same as that of SHPB when ignoring the difference of the incident impulse between BTIA and SHPB. The principle can be expressed by the Lagrange X–T sketch (shown in Fig. 1) which is based on the assumptions that:

1. stress wave propagation in the input/output bar is elastic and one-dimensional,
2. the stress and strain in the testing region of the specimen must be uniform and be under a unidirectional stress state.

According to the one-dimensional elastic stress wave theory, the predicted stress $\sigma(t)$, predicted strain $\varepsilon(t)$ and predicted strain-rate $\dot{\varepsilon}(t)$ in the specimen can be given by (Xia et al., 1996; Chen et al., 1995)

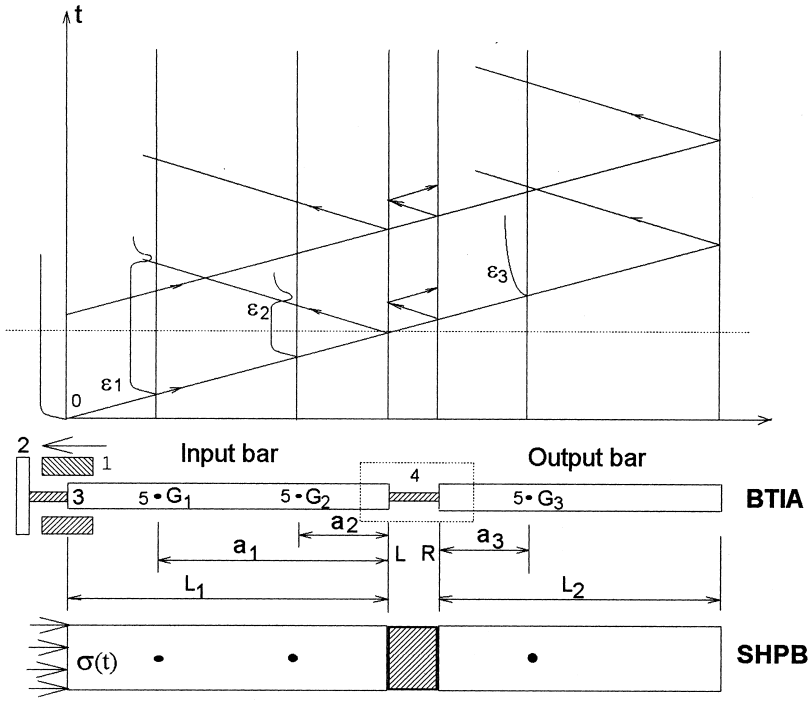

1. Hammer 2 .Block 3. Short metal bar 4. Specimen test region 5. strain gauges

Fig. 1. BTIA and SHPB and the Lagrange X–T sketch of the 1-D experimental measuring principle.

$$\sigma(t) = \frac{EA}{2A_s}[\varepsilon_i(t) + \varepsilon_r(t) + \varepsilon_t(t)], \tag{1}$$

$$\varepsilon(t) = \frac{C_0}{l_s}\int_0^t [\varepsilon_i(\xi) - \varepsilon_r(\xi)\varepsilon_t(\xi)]d\varsigma \tag{2}$$

and

$$\dot{\varepsilon}(t) = \frac{C_0}{l_s}[\varepsilon_i(t) - \varepsilon_r(t) - \varepsilon_t(t)] \tag{3}$$

Because $\varepsilon_i(t) + \varepsilon_r(t) = \varepsilon_t(t)$, Eqs. (1)–(3) can be simplified to

$$\sigma(t) = \frac{EA}{l_s}\varepsilon_t(t), \tag{4}$$

$$\varepsilon(t) = \frac{2C_0}{l_s}\int_0^t [\varepsilon_i(\xi) - \varepsilon_t(\xi)]d\xi \tag{5}$$

and

$$\dot{\varepsilon}(t) = \frac{C_0}{l_s}[\varepsilon_i(t) - \varepsilon_r(t)] \tag{6}$$

where A_s and l_s are the cross-sectional area and the length of the testing region of the specimen, respectively (Fig. 2). C_0, A and E are the one-dimensional elastic stress wave velocity, the cross-sectional area and Young's modulus of the input/output bars, respectively. ε_i, ε_r and ε_t are the incident strain signal and reflective strain signal in the input bar and the transmitted strain signal in the output bar measured by strain gauges, respectively.

In BTIA, two kinds of specimen and two methods of connection between specimen and input/output bar are used. The first uses a dumb-bell shaped cylindrical specimen, which should be connected to the input/output bar by a thread on the specimen. The other method uses a dumb-bell shaped flat specimen,

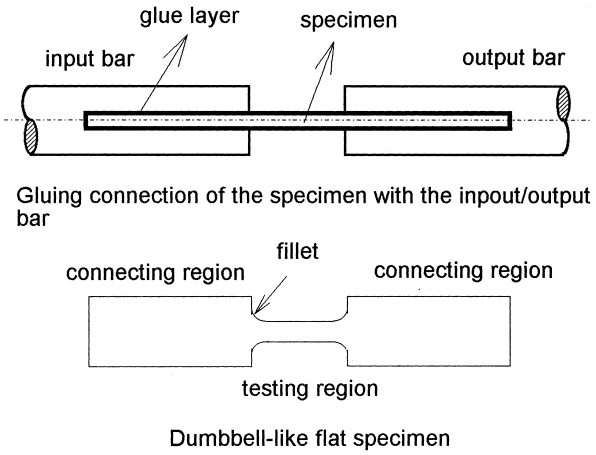

Fig. 2. Dumb-bell-shaped flat specimen and gluing connection.

which should be connected by glue. Compared with the SHPB system, in the BTIA system, the specimen and its connection with the input/output bars are more complicated, which may cause certain deviation from the assumptions adopted in the 1-D measuring principle.

Recently, we gave a two-dimensional axisymmetric numerical analysis for the BTIA system where dumb-bell shaped cylindrical specimens and threaded connections are used, and demonstrated the validity of the 1-D experimental measuring principle in the scope of elastoplastic theory (Wang et al., 1999; Wang, 1996). In that analysis, the threaded connection between the specimen and the input/output bar was assumed to be an ideal one (i.e. the displacements of both sides of the interfaces between the specimen and bar are compatible). During the actual experiment, the threaded connection often produces a larger predicted strain than the actual strain and may cause a non-constitutive oscillation in the $\sigma(t)$ and σ–ε curves (especially near the yield point). So, although the numerical analysis confirmed the validity of the one-dimensional principle used in the system, technical difficulties may hinder its usage.

At present, the authors' research group has adopted the second kind of specimen and the second method of connection, in which the dumb-bell shaped flat specimen is connected to the input/output bar with glue (Fig. 2) (Xia et al., 1996; Chen et al., 1995; Harding et al., 1982); a great number of experimental results confirmed its reliability. It is the objective of this paper to theoretically demonstrate the validity of the one-dimensional principle adopted in a BTIA using this kind of specimen and connection. However, the BTIA with a dumb-bell shaped flat specimen is more complicated and must use a three-dimensional dynamic FEM numerical analysis.

In the present paper, a simplified plane-symmetrical three-dimensional finite element model for a BTIA with a dumb-bell shaped flat specimen made of an elastoplastic material is first established. The numerical solution for the system under a stress impulse load on the left end-surface of the input bar is obtained by ADINA. In the scope of elastoplastic theory, the above mentioned principle can be demonstrated.

The process of demonstration is as follows. First, the constitutive relation of the specimen material selected for the simulative analysis in advance is called the 'input constitutive relation'. Second, through numerical solution of BTIA, the strain signals at the gauge positions on the input/output bar can be obtained. Using these strain signals, the predicted values of the specimen can be calculated, respectively, by Eqs. (1)–(3) or Eqs. (4)–(6). Third, through the numerical solution, the average values of the stress, strain and strain rate in the middle of the testing region of the specimen can be directly obtained, which are called the 'actual values' of the stress, strain and strain rate of the specimen. Thus, through calculation, one obtains two constitutive relations: the predicted one and the actual one. By comparison of these two relations and of the predicted values (stress and strain) with the actual ones, the validity of the one-dimensional experimental measuring principle can be demonstrated and discussed.

2. Three-dimensional finite element model and ADINA program

2.1. Three-dimensional finite element model

The BTIA with a flat specimen is simplified as a three-dimensional plane-symmetric model (shown in Fig. 3). G_1, G_2 and G_3 in Fig. 3 are three gauges on the input/output bars. The specimen which is made of elastoplastic material, is a flat dumb-bell shape consisting of a testing region, two connecting regions and two additional transitional fillets at the roots. A stress impulse ($P=\sigma_0 f(t)$, in which $f(t)$ is shown in Fig. 4) is uniformly applied on the end-surface of the input bar.

The stress on the right end-surface of the output bar and the other surface, i.e. the side surface and

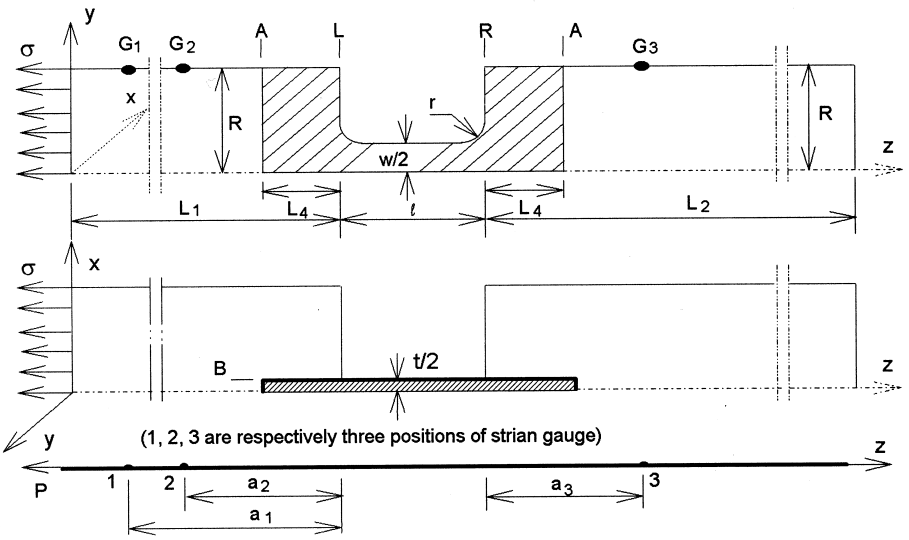

Fig. 3. Three-dimensional plane-symmetric model. (a) A part of the dumb-bell-like flat specimen. (b) Connection between the specimen and the input bar.

the surface at the varying section (L and R) are free. The force equilibrium and the continuous displacement condition at the interfaces between the specimen and bars are satisfied.

Due to the difficulties in constructing meshes near to the notches (Fig. 2), the model is simplified further as follows. The specimen (including the connecting and testing regions) is assumed to be under a plane-stress state, which is because the specimen is very thin and the stress wave propagating in the system is mainly longitudinal. The connection parts of the system (shown in Fig. 3 as part A to L and part R to A), which consist of the connection region of the specimen and end parts of the input/output bars, are simplified as cylinders without notch and with the same cross section as the bar, of which the physical parameters (density, Young's modulus, Poisson's ratio) can be calculated by mixed law:

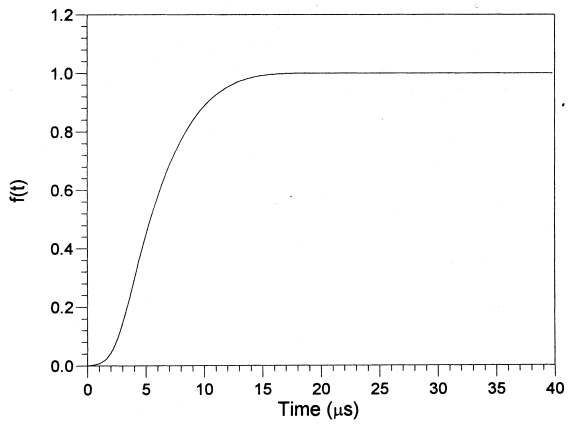

Fig. 4. Impulse load function $f(t)$.

$$X' = \left(\frac{\pi R^2 - 2RT}{\pi R^2}\right) X, \tag{7}$$

where R is the radius of the input/output bars, T is the thickness of the specimen, X' and X represent the equivalent parameters and the original parameters of the input/output bars in the connecting regions, respectively.

Based on the above simplification, the meshes of the model can be divided into the following parts: specimen, input/output bars and connection parts. The specimen mesh is constructed by 300 four-node and three-node plane-stress elements. The input/output bars are discretized by 1240 eight-node and six-node brick elements. The connection parts are discretized by 300 eight-node and six-node brick elements. Note that, for the specimen, the meshes of the specimen's connection region are the same as those of the YZ-plane of the connecting parts. Parts of the meshes for the model are present in Fig. 5(a,b).

The bars are made of a homogeneous isotropic linear elastic material. The Young's modulus (E), mass density (ρ) and Poisson ratio (ν) of the bars are shown in Table 2. A strain rate independent material (LY12cz Aluminum) is chosen as the specimen material in the present paper to avoid the effects of strain rate. Its constitutive relation can be simplified to form a hardening model (see Fig. 5) and the 1-D constitutive equation is

$$\sigma_y = \begin{cases} E\varepsilon & \sigma < \sigma_s \\ \sigma_s \varphi(\varepsilon) & \sigma \geq \sigma_s \end{cases}, \tag{8}$$

where E is Young's modulus, σ_y is yield stress and $\varphi(\varepsilon)$ is a rising and definitive function as ε increases. The deviatonic stress, S_{ij}, is limited by the Von Mises yield condition

$$S_{ij}S_{ij} \leq \frac{2}{3}\sigma_y^2, \tag{9}$$

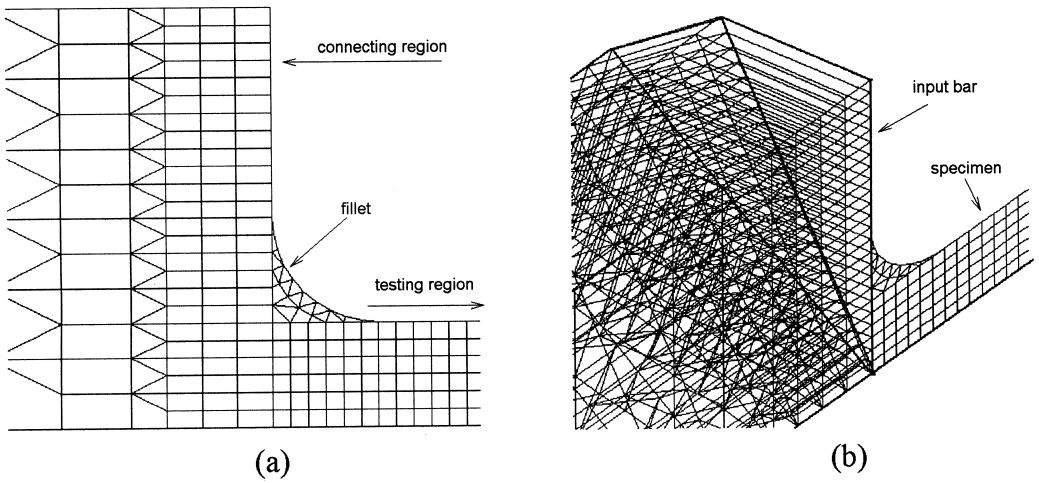

(a) a part of the dumbbell-like flat specimen

(b) Connection between the specimen and the input bar

Fig. 5. Finite element meshes of the region near the connecting region and the testing region. (a) A part of the dumb-bell-like flat specimen. (b) Connection between the specimen and the input bar.

where S_{ij} is

$$S_{ij} = \sigma_{ij} - \frac{\sigma_{mm}}{3}\delta_{ij}$$

and

$$\sigma_{mm} = \sum_{m} \sigma_{mm}. \tag{10}$$

2.2. Finite element ADINA program and its evaluation

The finite element program ADINA (Bathe, 1982, 1981) is used for numerical analysis in the present paper. Here, the implicit Newmark algorithm for integrating the governing equation with respect to time is employed. The spatially discretized equations of motion can be written as:

$$[M]\ddot{u} + [K]u = f, \tag{11}$$

where $[M]$ is the total consistent mass matrix, $[K]$ is the total stiffness matrix, u and $\ddot{u}$ are displacement and acceleration vectors, respectively and f is the external force vector.

In the implicit Newmark algorithm, the following assumptions are made:

$${}^{t+\Delta t}\dot{u} = {}^{t}\dot{u} + \left[(1-\delta){}^{t}\ddot{u} + \delta {}^{t+\Delta t}\ddot{u}\right]\Delta t \tag{12}$$

and

$${}^{t+\Delta t}u = {}^{t}u + {}^{t}\dot{u}\Delta t + \left[\left(\frac{1}{2} - \alpha\right){}^{t}\ddot{u} + \alpha {}^{t+\Delta t}\ddot{u}\right]\Delta t^2, \tag{13}$$

where, α and δ are two parameters to control the precision and stability of integration and $\delta = 0.54$,

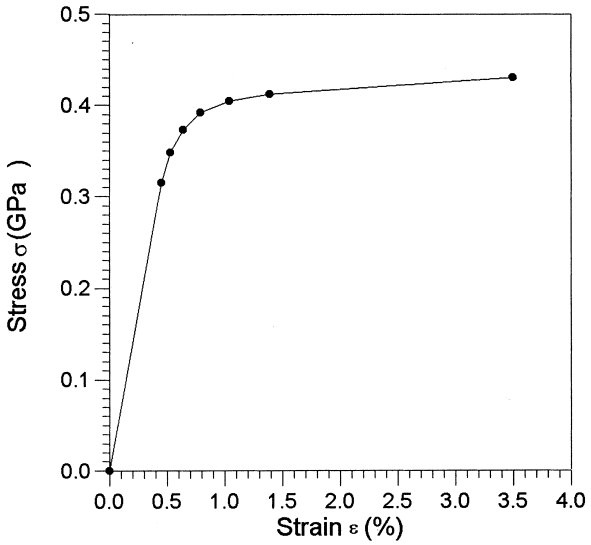

Fig. 6. Constitutive relation of the specimen material. (a) Non-homogenous bar. (b) Stress impulse function.

$\alpha = 0.25(0.5+\delta)^2$ are selected, which are proved to be suitable for the problem of the present paper by many evaluation examples.

Although ADINA (Wang, 1996; Wang et al., 1996, Wang et al., 1998; Wang and Xia, 1998) gave many detailed evaluations of solving dynamic nonlinear problems by the finite element method and the ADINA program, due to the complexity of the above-mentioned dynamic problem with several physical and geometric discontinuous faces, the feasibility of solving the dynamic problem by the finite element ADINA program has to be checked. Below is one of the samples we used for evaluating the program.

Fig. 7(a) shows a non-homogenous bar with interior interfaces which consists of an input bar with round cross-section and an output bar with rectangular cross-section. The plane ($z = L_1 - L_3$) and the plane ($x = T/2$) are called the interior interfaces. The full region L_3 is called the connecting region and its relevant parameters are shown in Table 1. The left end-surface of the input bar is applied by a uniform stress impulse ($\sigma_z = \sigma_0 f(t)$, $\sigma_0 = 0.2$ GPa and $f(t)$ is shown in Fig. 7(b) with 10 μs rise time). The model is stationary at initial time.

The simplification the meshes of the model are similar to those in Section 2.1. Suppose that the Poisson's ratio of the model is zero ($\nu_1 = \nu_2 = 0$), i.e. neglecting the transverse inertia of the model. Through the numerical analysis by the finite element ADINA program, the axial stress at two points (z = 120 mm and z = 360 mm) on the surface of the bar are shown in Fig. 8.

As a comparison, the system is analyzed by means of the one-dimensional analysis method. The input bar, the connecting region and the output bar in the model are defined as regions I, II and III, respectively. Here, region II is simplified as an equivalent homogenous material and its relevant material parameters can be gained by the mixed law: $x = V_1\ x_1 + V_2 x_2$, where x is the equivalent parameter, V_1 and V_2 are the volume fractions of material x_1 and material x_2, respectively. According to the 1-D stress wave theory, after the stress wave is reflected and transmitted n times through the connecting region, the stresses in region I and region III can be obtained (Wang and Xia, 1998) as follows:

$$\sigma_1^{(n)} = \left[(1+\beta_{12}) + \alpha_{21}\beta_{23}\alpha_{12} \sum_{m=1}^{n} (\beta_{21}\beta_{23})^{m-1} \right] \sigma_0 \tag{14}$$

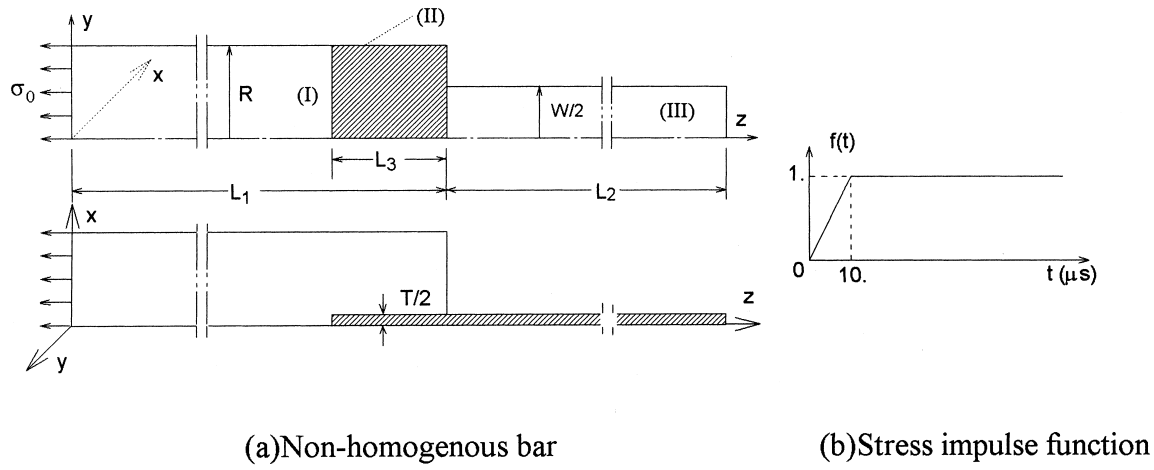

Fig. 7. Model for the non-homogenous bar with interior interfaces. (a) Non-homogenous bar. (b) Stress impulse function.

Table 1
Relevant parameters of the bar

	E (GPa)	ρ (Kg/m^3)	ν (mm)	L (mm)	R (mm)	W (mm)	T (mm)
Input bar	200	8000	0.0	240	6		
Flat bar	50	2000	0.0	240		3	1

and

$$\sigma_3^{(n)} = \left[\sum_{m=1}^{n+1} \alpha_{12}\alpha_{23}(\beta_{21}\beta_{23})^{(m-1)}\right]\sigma_0, \tag{15}$$

where, α_{12}, α_{23} and α_{21} are the transmission parameters of a stress wave transmitted from region I to region II, from region II to region III and from region II to region I, respectively. β_{12}, β_{23} and β_{21} are the reflection parameters of a stress wave reflected from region I to region II, from region II to region III and from region II to region I, respectively; σ_0 is the incident stress impulse. The one-dimensional solution for the problem is also shown in Fig. 8.

Fig. 8 shows that the 3-D numerical result is nearly the same as the 1-D equivalently simplified solution, which confirms the feasibility of analysing the BTIA dynamic system with several physical and geometric discontinuous faces by the finite element method and the ADINA program.

3. Demonstration of the validity of the 1-D experimental measuring principle

As the connecting region forms a full transverse constraint in the roots of the testing region, in general, the length-to-width ratio of the testing region in BTIA (Xia et al., 1989, 1992, 1993) is rather bigger than that in SHPB in order to ensure a good unidirectional stress field in the testing region. Hence, in the present paper, we select the geometric and physical parameters of the specimen and the

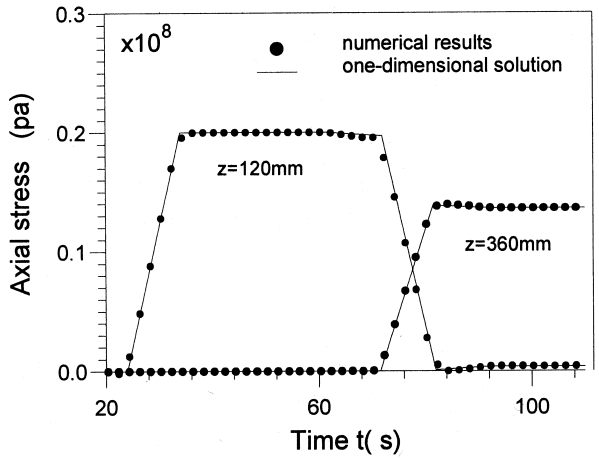

Fig. 8. Stress history at two special positions in the bar.

Table 2
Geometric parameters and material parameters of the model

Material parameters of the model			E (GPa)	ρ (kg/m^3)	ν
Input/output bars			200	8000	0.25
Specimen			70	2700	0.32
Geometric parameters of the model					
Input bar (mm)	Output bar (mm)	Testing region (mm)	Connecting region (mm)	Fillet (mm)	Specimen's thickness (mm)
$L_1 = 360$	$L_2 = 360$	$l = 12$	$L_4 = 26$	$R = 1$	$t = 1$
$R_1 = 6$	$R_2 = 6$	$w = 3$	$a_1 = 120$	$a_2 = 240$	$a_3 = 120$

input/output bar as listed in Table 2. Through the implementation of ADINA, the strain signals (shown in Fig. 1) at the gauge positions G_1, G_2 and G_3 can be obtained (shown in Fig. 9).

3.1. Stresses and strains distributions in the testing region of the specimen with fillets

The stress and stain distributions and the ratio of the maximum non-axial stress to the average axial stress in the testing region at $t = 140$ μs (when the testing region is in the plastic state and the strain value in the middle of testing region is about 3%) are summarized in Figs. 10 and 11. Where $\sigma_z^{\max}(\varepsilon_z^{\max})$ represents the maximum axial stress (strain), $\max(\sigma_{ij})$ represents the maximum non-axial stress and $\bar{\sigma}_z(\bar{\varepsilon}_z)$ represents the average stress and strain in the corresponding cross-section, respectively. Fig. 10(a) indicates that along the longitudinal direction, the values of $(\sigma_z^{\max} - \bar{\sigma}_z)/\bar{\sigma}_z$, $\max(\sigma_{ij})/\bar{\sigma}_z$ and $(\varepsilon_z^{\max} - \bar{\varepsilon}_z)/\bar{\varepsilon}_z$ in 85% of the testing region are less than 5%.

The ratio of the average axial stress (strain) in the testing region to the axial stress (strain) in the mid cross-section of the testing region at $t = 140$ μs are summarized in Fig. 10(b), where $\bar{\sigma}_z(\bar{\varepsilon}_z)$ represents the

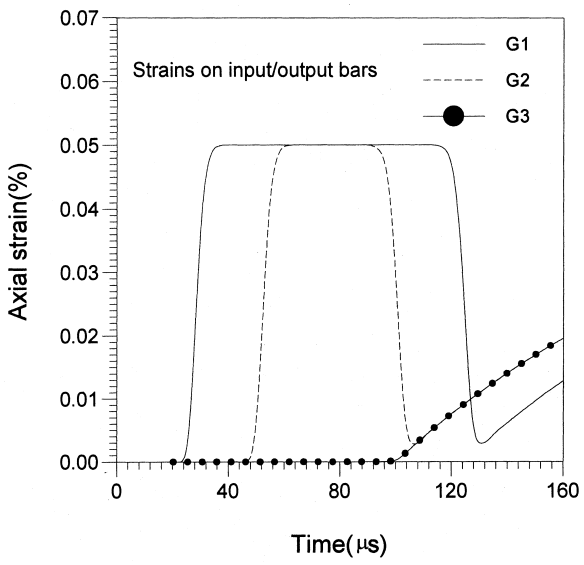

Fig. 9. Strain signals on the input/output bar.

average axial stress (strain) and $\bar{\sigma}_z^{\mathrm{mid}}(\bar{\varepsilon}_z^{\mathrm{mid}})$ represents the average axial stress (strain) in the middle cross-section of the testing region, respectively. Fig. 10(b) indicates that along the longitudinal direction, the value of $(\bar{\sigma}_z - \bar{\sigma}_z^{\mathrm{mid}})/\bar{\sigma}_z^{\mathrm{mid}}$ in 95% of the testing region is less than 5% and the value of $(\bar{\varepsilon}_z - \bar{\varepsilon}_z^{\mathrm{mid}})/\bar{\varepsilon}_z^{\mathrm{mid}}$ in 75% of the testing region is less than 5%.

The uniformity of stress and strain in the testing region with respect to time is summarized in Fig. 11, where $\bar{\sigma}_z^{\max}(\bar{\varepsilon}_z^{\max})$ represents the maximum average axial stress (strain) among various cross-sections in the testing region. $\bar{\sigma}_z^{\mathrm{tot}}(\bar{\varepsilon}_z^{\mathrm{tot}})$ represents the average axial stress (strain) in the testing region. Fig. 11

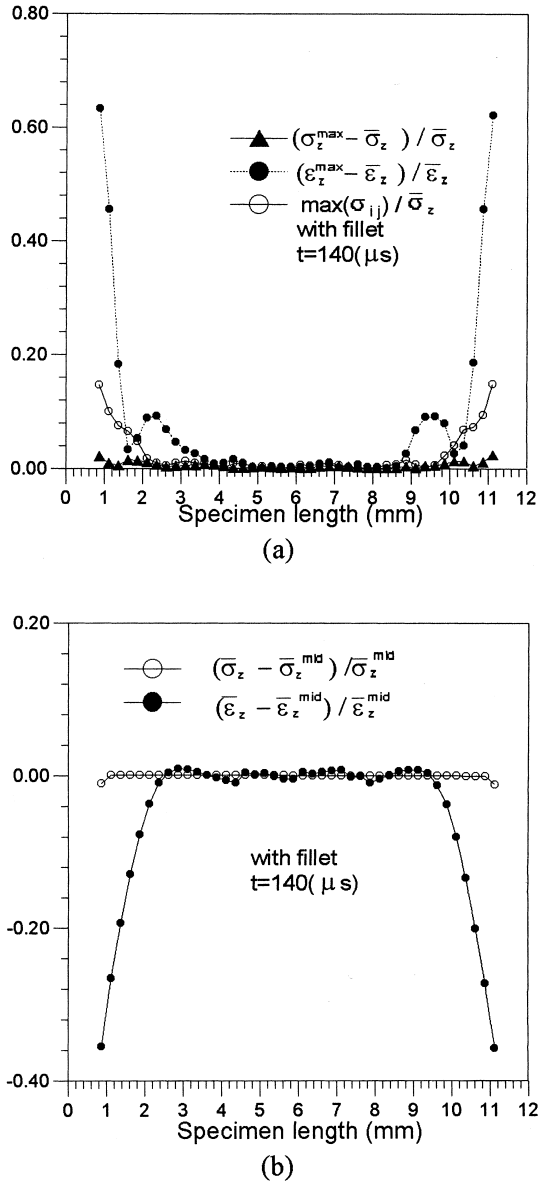

Fig. 10. Uniformity of stress and strain, and unidirectionality of stress in the testing region.

indicates that the axial stress (strain) distribution is non-uniform in the beginning microseconds after the stress (strain) wave approaches the testing region while, after several microseconds, during which the waves reflect and transmit in the testing region, the distributions become uniform. Therefore, the nonuniformity of stress (strain) in the testing region hardly has any influence on the experimental results.

As analyzed above, it is clear that when the middle of the testing region has a suitable length-to-width ratio, its stress and strain fields are approximately uniform and under a unidirectional stress state. The axial stress is rather greater than the non-axial stresses. The non-uniform stress and strain regions are only located in the roots of the testing region. In a word, the assumptions (i.e. the uniformity of stress and strain under a unidirectional stress state in the middle of the testing region except fillets) in the 1-D experimental measuring principle can be approximately satisfied for the specimen with matched geometric sizes. Thus, the average values of the physical parameters, such as strain, stress etc., in the middle of the testing region obtained by the numerical analysis can be regarded as the actual values of the corresponding physical parameters of the specimen.

3.2. Distortion of cross-sections (L and R) and the stress concentration in the roots of the testing region and its elimination

Here, the model without fillets is also analyzed and its numerical results are compared with those of the model with fillets.

Figs. 12 and 13 show the displacement distribution on the L and R cross-sections at $t = 140$ μs, which indicates that, compared with the specimen with fillets, the distortion of the cross-sections is more remarkable for the specimen without fillets.

Fig. 14 shows the stress distribution on the L and R cross-sections at $t = 140$ μs and indicates that dramatic stress concentration exists in the concave location of the roots of the testing region for the model without fillets while, for the model with fillets, the stress concentration in the roots of the testing region disappears.

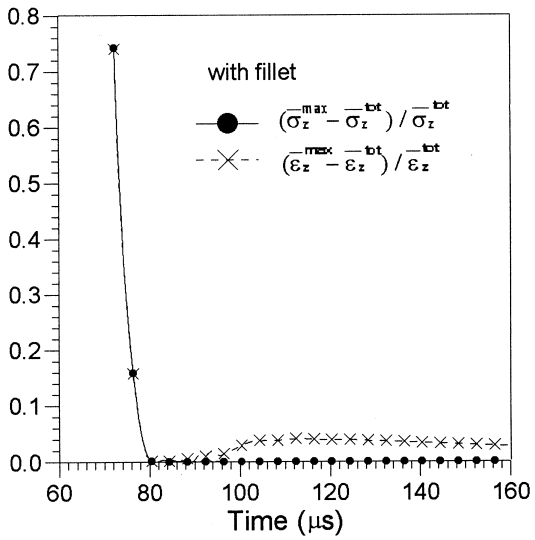

Fig. 11. Uniformity of stress and strain with time.

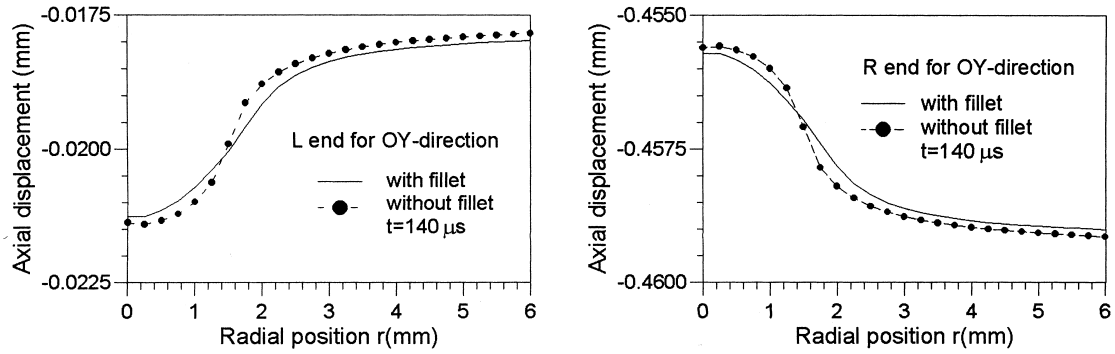

Fig. 12. Axial displacement along OY-direction on cross-sections (L and R).

3.3. The comparison of the predicted values with the actual values (stress, stain and strain rate)

The comparison of the actual values and the predicted values (such as stress, strain, and strain-rate and constitutive relation) obtained from Eqs. (4)–(6) for the specimens with and without fillets is summarized in Figs. 15–18.

Fig. 15 shows that the predicted stress coincides well with the real stress, regardless of whether the specimen has fillets or not, which indicates that the fillets have little influence on the precision of the predicted stress. However, only the specimen with fillets can be adopted in the actual tensile impact experiment in order to avoid the specimen breaking at the roots of the testing region.

Fig. 16 shows that for the specimen without fillets, the predicted strain is greater than the actual strain and the difference becomes bigger as time increases, but for the specimen with fillets, the predicted strain is identical with the actual strain. This is because the predicted strain is dependent on the relative displacements between the L and R cross-sections and the length of the testing region. If the specimen has no fillets, both the distortion on the L and R cross-section and the relative displacements between them are slightly larger. Thus, in order to reduce the difference between the predicted and actual stain, the distortion on the L and R cross-sections must be reduced (but the distortion cannot be eliminated completely) and the rigidity in the roots of the testing region must be strengthened to partially counteract the relative displacement between the L and R cross-sections. The method of adding the fillets can achieve these above mentioned aims.

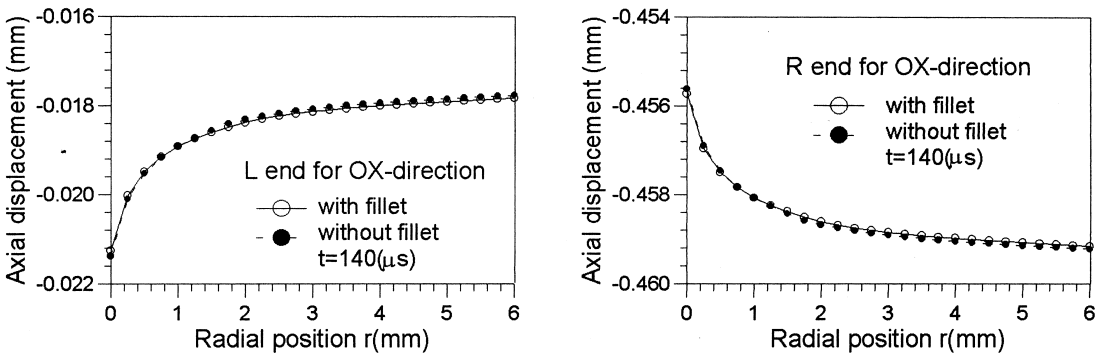

Fig. 13. Axial displacement along OX-direction on cross-sections (L and R).

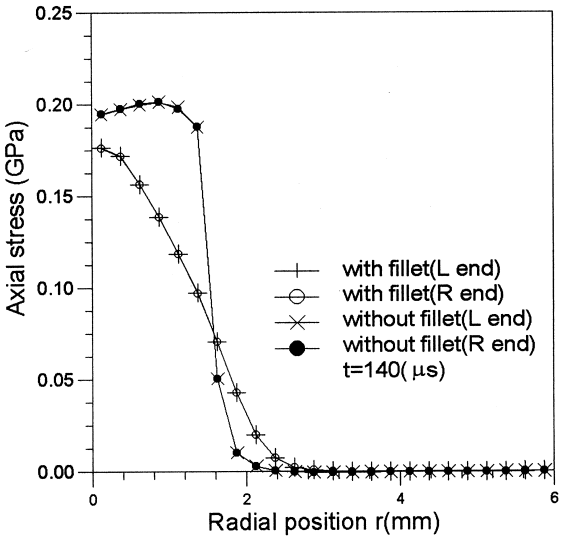

Fig. 14. Stress distribution along OY-direction on cross-sections (L and R).

Fig. 17 shows that the predicted constitutive relation coincides with the real constitutive relation for the specimen with fillets. Fig. 18 indicates that the predicted strain-rate for the specimen with fillets and the BTIA test can be approximately considered as a constant strain-rate test (strain rate is 590/s).

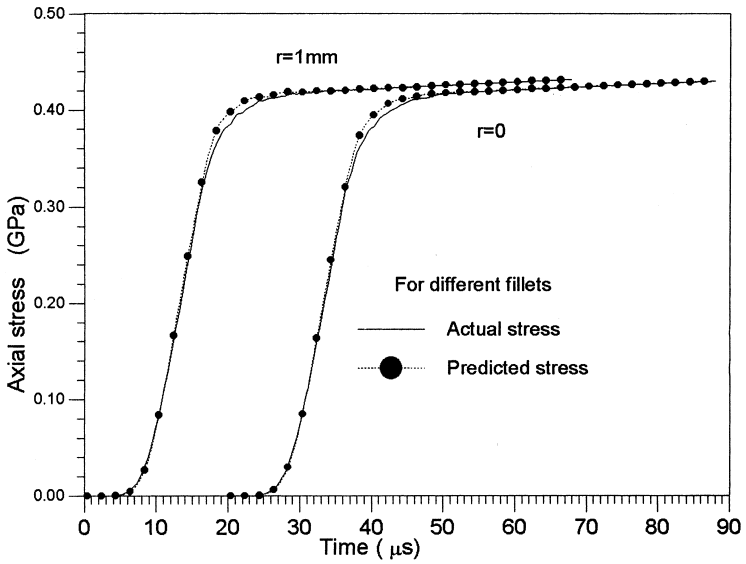

Fig. 15. Specimen stress history.

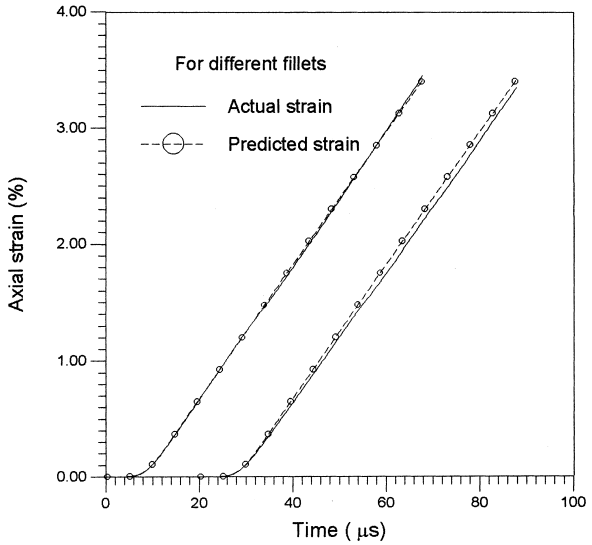

Fig. 16. Specimen strain history.

3.4. Influence of the strain-rate on the predicted stress and strain

By way of changing the amplitude σ_0 in $P=\sigma_0 f(t)$, the strain rates of the simulative tests can be changed. For the above mentioned model with fillets, the BTIA testing process at different strain rate are simulated by selecting different input impulse amplitudes ($\sigma_0=0.1$ GPa, 0.15 GPa and 0.25 GPa). The simulative experimental results are listed in Figs. 19 and 20, in which curves 1, 2 and 3 are for the different amplitudes ($\sigma_0=0.1$ GPa, 0.15 GPa and 0.25 GPa correspond to strain rates of 350/s, 590/s and 1000/s, respectively).

From Figs. 19 and 20, the strain-rate has little influence on the predicted stress and the influences are mainly concentrated near to the initial yield. The agreement between predicted and actual strains decreases when the strain rate increases. For the case of the 1000/s strain-rate, the predicted stress is more than the actual stress in the stage of the initial yield. This is because the higher the strain-rate, the

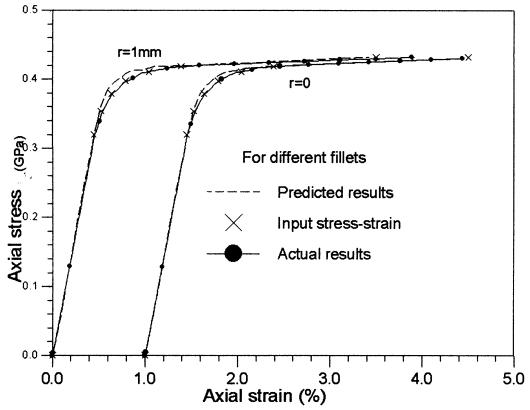

Fig. 17. Specimen stress–strain relation.

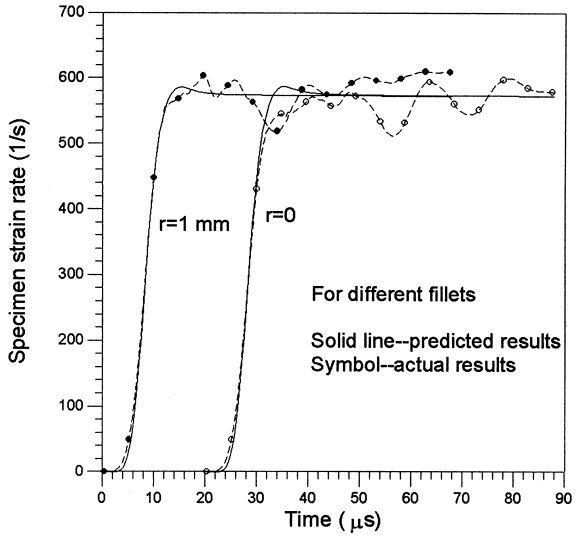

Fig. 18. Strain-rate history.

larger the influence of the connecting region on the predicted stress. In order to improve the predicted stress, the length of the connecting region is changed to 15 mm. The BTIA test with the 1000/s strain-rate is numerically simulated again, and the result (curve 4) is shown in Figs. 19 and 20. The comparison of curve 4 with curve 1 indicates that the predicted stress is improved. In addition, Fig. 20 indicates that, in general, the strain-rate slightly influences the predicted strain.

3.5. Foundations for the validity of the 1-D experimental principle

All of the analyses in the above sections indicate that the one-dimensional measuring principle adopted in a BTIA is valid. The foundations making the principle valid can be concluded as follows:

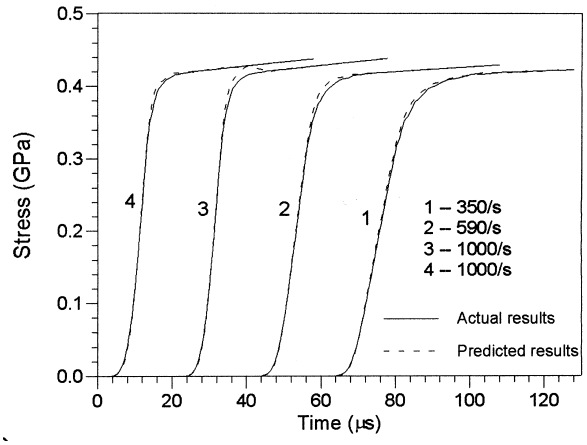

Fig. 19. Specimen stress history.

1. A uniform stress and strain region, existing within a unidirectional stress state, must be formed in the middle of the testing region.
2. By adding fillets in the roots of the testing region, the stress concentration in the roots can be partially eliminated. Meanwhile, adding fillets can debase the distortion of the L and R cross-sections, so as to reduce and counteract the relative displacement between them. Thus, the precision of the predicted stain is improved.
3. The average value of stress and strain (the actual value) in the uniform middle of the testing region should coincide with the predicted value.

4. Conclusions and recommendations

1. In the scope of elastoplastic theory, the present paper preliminary demonstrates the validity of the 1-D experimental principle, confirms that the assumptions in the 1-D experimental measuring principle are approximately satisfied and gives foundations for the validity of the 1-D experimental principle.
2. In order to make the 1-D experimental principle valid, it is essential to rationally select the specimen shape and geometric size. The matched relations between the specimen's geometric size and the experimental system can be found through the numerical simulation. Due to limited space, this problem is not discussed in the present paper.
3. In the present paper, since the connection between the dumb-bell-like flat specimen and the input/output bar in the model is simplified, the influence of the glue layer on the 1-D experimental measuring principle is not considered in the model. In addition, the simplification of the connecting regions and the specimen may have an effect on the predicted strain. These will be studied further.

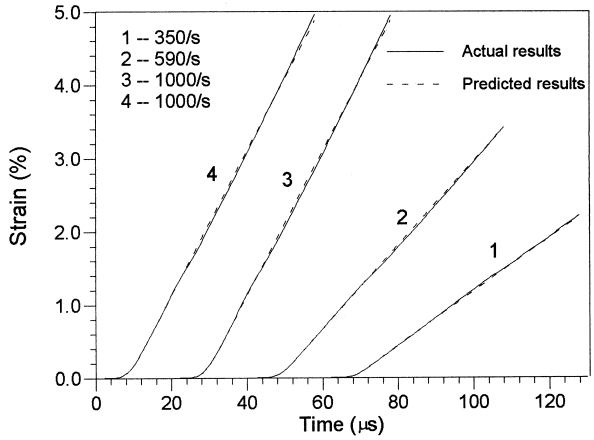

Fig. 20. Specimen strain history.

Acknowledgements

The research work in the present paper was supported by the National Natural Science Foundation of the People's Republic of China.

References

Bathe, K.J., 1981. ADINA—a Finite Element Program for Automatic Dynamic Incremental Nonlinear Analysis. Massachusetts Institute of Technology, Cambridge, Massachusetts Reports AE81-1, AE81-2, AE81-3, September 1981.

Bathe, K.J., 1982. Finite Element Procedures in Engineering Analysis. Prentice–Hall, Inc, Englewood Cliffs, New Jersey 07632.

Bertholf, L.D., 1974. Feasibility of two dimensional numerical analysis of the Split–Hopkinson Pressure Bar System. Journal of Applied Mechanics Series E, No. 1 41, 137–144.

Bertholf, L.D., Karnes, C.H., 1975. Two-dimensional analysis of the Split–Hopkinson Pressure Bar system. J. Mech. Phys. Solids 23, 1–19.

Chen, Y., Tu, Z.H., Yang, B.C., 1995. Study of dynamic and mechanical behavior of Sic/Al composite under tensile impact. Applied Composite Materials 2, 43–50.

Harding, J., et al., 1982. Impact testing of fibre-reinforced composite materials. In: Proc. ICCM—IV, Tokyo, p. 845.

Kolsky, H., 1949. An investigation of the mechanical properties of materials at very high rates of loading. Proc. Phys. Soc. (London) Ser. B. 62, 676–700.

Wang, C.Y., 1996. Dynamic Numerical Analysis for Bar–Bar Tensile Impact Testing System—Demonstration for Experimental Measuring Principle and Matching Relation among Specimen's Geometric Sizes. Ph.D. Thesis, University of Science & Technology of China.

Wang, C.Y., Wan, H.P., Xia, Y.M., 1999. Two-dimensional axisymmetric numerical analysis of Bar–Bar Tensile Impact Apparatus by elastoplastic FEM. Journal of Sound and Vibration 220 (15), 787–806.

Wang, C.Y., Xia, Y.M., 1998. Reflection and transmission of the elastic waves in the bar with unhomogeneous regions and various sections. Chinese Journal of Applied Mechanics 15 (3), 44–50.

Wang, C.Y., Xia, Y.M., et al., 1996. Two-dimensional finite element analysis of elastic wave propagation in cylindrical bars with interfaces. Journal of China University of Science and Technology 26, 64–69.

Xia, Y.M., et al., 1992. Rotating disc bar–bar tensile impact test apparatus and its experimental technique. In: Science and Technology Achievement Appraisal, vol. 92. National Natural Science Foundation of P.R. China.

Xia, Y.M., Yang, B.C., Jia, D.X., Dong, L.M., 1989. Pendulum bar–bar tensile impact test apparatus and dynamic technique of measuring low temperature. Experimental Mechanics 4, 57–66.

Xia, Y.M., Wang, X., Yang, B.C., 1993. Brittle–ductile–brittle transition of glass fibre-reinforced epoxy under tensile impact. Journal of Materials Science Letters 12, 1481–1484.

Xia, Y.M., Wang, X., Yang, B.C., 1996. Constitutive equation for unidirectional composites under tensile impact. Composites Science and Technology 56, 155–160.